Nanoscale

PAPER

View Article Online
View Journal | View Issue

Cite this: *Nanoscale*, 2014, **6**, 4830

Cost-effective and eco-friendly synthesis of novel and stable N-doped ZnO/g-C_3N_4 core–shell nanoplates with excellent visible-light responsive photocatalysis†

Santosh Kumar,[a] Arabinda Baruah,[b] Surendar Tonda,[a] Bharat Kumar,[b] Vishnu Shanker*[a] and B. Sreedhar[c]

Received 3rd October 2013
Accepted 5th February 2014

DOI: 10.1039/c3nr05271k

www.rsc.org/nanoscale

N-doped ZnO/g-C_3N_4 hybrid core–shell nanoplates have been successfully prepared *via* a facile, cost-effective and eco-friendly ultrasonic dispersion method for the first time. HRTEM studies confirm the formation of the N-doped ZnO/g-C_3N_4 hybrid core–shell nanoplates with an average diameter of 50 nm and the g-C_3N_4 shell thickness can be tuned by varying the content of loaded g-C_3N_4. The direct contact of the N-doped ZnO surface and g-C_3N_4 shell without any adhesive interlayer introduced a new carbon energy level in the N-doped ZnO band gap and thereby effectively lowered the band gap energy. Consequently, the as-prepared hybrid core–shell nanoplates showed a greatly enhanced visible-light photocatalysis for the degradation of Rhodamine B compare to that of pure N-doped ZnO surface and g-C_3N_4. Based on the experimental results, a proposed mechanism for the N-doped ZnO/g-C_3N_4 photocatalyst was discussed. Interestingly, the hybrid core–shell nanoplates possess high photostability. The improved photocatalytic performance is due to a synergistic effect at the interface of the N-doped ZnO and g-C_3N_4 including large surface-exposure area, energy band structure and enhanced charge-separation properties. Significantly, the enhanced performance also demonstrates the importance of evaluating new core–shell composite photocatalysts with g-C_3N_4 as shell material.

1. Introduction

In recent years, semiconductor photocatalysis technology has attracted considerable interest for environmental remediation, for example for air and water remediation, as well as for clean energy production, for example hydrogen energy production by water splitting, because solar energy is readily available, cost-free, environmental-friendly, and a renewable energy source.[1–4] To date, a large number of semiconductor materials have been studied for environmental remediation and water-splitting.[3,5–7] Among them, ZnO has been extensively studied due to its fascinating features including wide band gap, cost-free, non-toxicity, high electron mobility and high efficiency.[3,8,9] Unfortunately, ZnO is active in only UV light. One of the potential pathways for achieving high visible-light efficiency is to shift its absorption form the UV region into the visible region, for receiving and utilizing solar energy. Many efforts have been made to improve the visible-light active photocatalysis of ZnO by doping with metal and non-metal ions, co-doping with two or more ions, surface sensitization with organic dye or metal complex and coupling with metal or another semiconductor.[8,10,11] However, the metal and non-metal doping have attracted remarkable attention.[12,13] In particular, N-doping is thought to be the most suitable p-type dopant due to the both atomic size and electronic structure considerations. The nitrogen atom is closest in atomic size and electronegativity to oxygen and therefore, it results minimum strain in ZnO. Moreover, a small formation energy is required for the substitution of O in ZnO. Due to these features N-doping has been successfully applied to ZnO for visible-light photocatalysis.[13–15] However, N-doped ZnO did not exhibit much photocatalytic efficiency unlike widely studied N-doped TiO_2 counterpart.[16] It is also well known that ZnO usually suffers from serious photocorrosion in long term photocatalytic processes.[17–19] Therefore, the strategies for making ZnO a visible-light active photocatalyst have been continuously pursued.

On the other hand, coupling with a metal or another semiconductor which exerts a substantial influence in modifying the electronic band structure and construction of favourable surface structure in semiconductors, resulting in high quantum

[a]*Department of Chemistry, National Institute of Technology, Warangal-506004, A.P., India. E-mail: vishnu@nitw.ac.in; Fax: +91-870-2459547; Tel: +91-870-2462675*

[b]*Department of Chemistry, Indian Institute of Technology Delhi, New Delhi-110016, India*

[c]*Inorganic and Physical Chemistry Division, Indian Institute of Chemical Technology, Hyderabad-506004, A.P., India*

† Electronic supplementary information (ESI) available. See DOI: 10.1039/c3nr05271k

efficiency for photocatalytic reactions has been also extensively investigated.[20] ZnO based heterostructures such as ZnO/CdS, ZnO/CuO, ZnO/GaN, and ZnO/reduced graphene oxide have been actively studied and show the ability to improve the photocatalytic activity of ZnO under visible-light irradiation by extending its absorption range to visible-light region and promoting the photoinduced charge carrier transfer process.[10,11,21,22] For heterostructured photocatalysts besides the prolong life time of charge carrier transfer, two more aspects can also play important role in determining the photocatalytic efficiency in particular for long term applications. One is the photostability of different semiconductor materials in heterostructure. The other is the effective contacting between two materials in heterostructure. The intimate and lasting contact can effectively promote the photoinduced charge charier transfer between different semiconductor materials in heterostructures and consequently, achieve a higher photocatalytic activity. One of these drawbacks or both together have been observed in the traditional ZnO based heterostructures. Therefore, the performance of present ZnO based photocatalysts does not meet the needs of practical applications. As a result, the development of a new efficient photocatalyst or the modification of existent ones is still in progress.

More recently, graphitic carbon nitride (g-C_3N_4) a typical metal-free polymeric semiconductor material has attracted a great deal of scientific interest in photocatalytic water splitting and degradation of environmental pollutants under visible-light irradiation due to its suitable band gap to absorb the visible-light and unique properties.[23–25] However, the efficiency of this metal-free polymeric photocatalyst is still limited due to the high recombination rate of photogenerated electron–hole pairs, and the low surface area which make it inefficient to absorb visible-light effectively. Therefore, coupling with N-doped ZnO nanoplates makes g-C_3N_4 a valuable material for visible light driven photocatalysts. The combination of these two photocatalysts is of potential interest for overall water splitting under solar light since g-C_3N_4 is a newly developed metal free hydrogen evolution photocatalyst, whereas the N-doped ZnO could serve as water oxidation photocatalyst.

In principle, core–shell heterostructures have the obvious merit of forming more favourable interface combination and superior charge transport capability by lowering grain boundary recombination.[25–27] Moreover, the interactions between different semiconductor materials of the core and shell can significantly improve the overall performance including long-term photostability of core of the core–shell heterostructures and even produce beneficial synergistic effects.[28] It is also important to promote the direct Z-scheme charge carrier transfer process by creating a favorable interface in core–shell heterostructures.[29] Significantly, the evaluation of potential photocatalytic Z-schemes is of critical importance given the growing need for an efficient and inexpensive means of harnessing the huge energy potential of solar irradiation to drive chemical reactions such as clean hydrogen energy from water splitting and the degradation of organic pollutants.[30–32]

Herein we report a facile, cost-effective and eco-friendly synthesis of novel and stable N-doped ZnO/g-C_3N_4 hybrid core–shell photocatalyst with Z-scheme mechanism to achieve the improved visible-light responsive photocatalysis by prolong life time of charge carrier transfer. The novel N-doped ZnO/g-C_3N_4 organic–inorganic hybrid nanoplates were characterised by powder X-ray diffraction (XRD), Thermogravimetric analysis (TGA), UV-Vis diffuse reflectance spectroscopy (UV-Vis DRS), Fourier transform infrared spectroscopy (FTIR), scanning electron microscopy (FESEM), energy dispersive elemental spectroscopy (EDX), transmission electron microscopy (TEM), X-ray photoelectron spectroscopy (XPS), electron spin resonance (ESR), photoluminescence (PL) and surface area analyser. Based on our experimental results, a proposed mechanism is discussed for enhanced visible-light photocatalysis. However, to the best of our knowledge there is no report on the synthesis of N-doped ZnO/g-C_3N_4 organic–inorganic hybrid nanocomposite photocatalyst.

2. Experimental details

2.1 Materials

Melamine (Aldrich, 99.0%), zinc nitrate (Aldrich, 99.0%), ammonium oxalate (Aldrich, 99.0%), and Rhodamine B (Aldrich, 85.0%) were used as received. All other reagents used in this work were of analytically pure and used without further purification.

2.2 Method

2.2.1 Preparation of bulk g-C_3N_4 and g-C_3N_4 nanosheet. Bulk g-C_3N_4 was prepared by direct heating melamine to 550 °C for 2 h in N_2 atmosphere and named as BCN.[33] Pure g-C_3N_4 nanosheet is prepared by liquid phase exfoliation. In brief, 0.05 g of g-C_3N_4 was ultrasonicated in 50 mL of water for 1 h and centrifuged to remove the unexfoliated g-C_3N_4. This pure g-C_3N_4 nanosheet is named as CNNS.

2.2.2 Preparation of pure ZnO nanoparticles and N-doped ZnO nanoplates. The ZnO nanoplates were prepared by using a co-precipitation method. 0.1 M metal precursor solution was directly mixed with 0.1 M aqueous solution of ammonium oxalate while stirring and kept for 1 h at room temperature. The solution became cloudy and a white precipitate of zinc oxalate was obtained. The oxalate precursor was centrifuged, washed (thrice) with water and ethanol and dried at 80 °C for 1 h. Furthermore, the oxalate precursor calcined at 500 °C for 12 h to obtain the ZnO nanoparticles. For the preparation of N-doped ZnO nanoplates, the oxalate precursor was mixed and grinded well with urea and calcined under same experimental conditions. Here, the pure ZnO is named as ZO and N-doped ZnO is named as ZON.

2.2.3 Preparation of N-doped ZnO/g-C_3N_4 hybrid nanoplates. In brief, an appropriate amount of g-C_3N_4 was ultrasonicated in 50 mL of water for 1 h. To this dispersion, 0.1 g of N-doped ZnO was added and stirred for 48 h. After evaporation of the water, a powder sample of N-doped ZnO/g-C_3N_4 nanoplates were obtained and dried at 100 °C for 1 h. The N-doped ZnO/g-C_3N_4 nanoplates with 5 wt% loaded g-C_3N_4 are named as CNZON5 and 10 wt% loaded g-C_3N_4 are named as CNZON10.

2.3 Characterization

X-ray diffraction studies (XRD) were carried out on a Bruker D8 Advance diffractometer using Ni filtered Cu Kα radiation. Thermo gravimetric and differential thermal analysis (TG/DTA) was carried out on PerkinElmer Pyris Diamond TGA/DTA system on well ground samples in flowing nitrogen atmosphere with a heating rate of 10 °C min^{-1}. The Fourier transform infrared (FTIR) spectra were recorded in transmission mode from 4000 to 400 cm^{-1} on a Nicolate Protégé 460 FTIR spectrometer using KBr discs. Field emission scanning electron microscopy (FESEM) studies of samples were carried out on a FEI quanta 3D FEG-FESEM operated at 10 kV by coating the powder sample with gold. Transmission electron microscopy (TEM) was done on a JEOL, JSM-6700F instrument. Chemical compositions of the samples were analysed by X-ray photoelectron spectroscopy (Kratos Axis ULTRA incorporating a 165 mm hemispherical electron energy analyzer). Electron spin resonance measurements were recorded with a Bruker A300E spectrometer. UV-Vis diffuse reflectance spectra were recorded on a Lambda/20 Instruments (UV-Vis NIR spectrophotometer), equipped with an integrating sphere to record the diffuse reflectance spectra of the samples, and $BaSO_4$ was used as a reference. The nitrogen adsorption–desorption isotherms were recorded by using Quanta chrome NOVA 1200e. The photoluminescence (PL) spectra were recorded on TSC solutions F96PRO fluorescence spectrophotometer with excitation wavelength of 365 nm.

2.4 Photocatalytic activity

Rhodamine B (RhB), a widely used dye, was chosen as a model pollutant to examine the visible-light responsive photocatalysis of the different samples. The photocatalytic activity of all the prepared samples (0.025 g) was evaluated for the degradation of RhB aqueous solution (100 mL, 5 mg L^{-1}) in a beaker under stirring condition at 250 rpm throughout the test at room temperature under visible-light irradiation. The visible-light source for the photo-irradiation is a solar simulator 300 W Xe lamp (Asahi Spectra Co., Ltd) with a super cold filter, which provides the visible light region ranging from 400 nm to 700 nm and a light intensity of 115 mW cm^{-2}. Prior to irradiation, solutions suspended with photocatalysts were stirred in dark condition for 30 min to ensure that the surface of the catalyst was saturated with RhB. During photocatalytic processes, the sample was periodically withdrawn, centrifuged to separate the photocatalyst from the solution, and used for the absorbance measurement. The absorption spectra were recorded on a UV-Vis spectrophotometer. The photocatalytic activity of the novel hybrid core–shell nanoplates compared with the pure ZnO, pure g-C_3N_4 and N-doped ZnO powders under the same experimental conditions.

2.5 Detection of reactive species

The reactive species detection process is similar to the photodegradation experimental process. Various scavengers were subjected into the RhB solution prior to addition of photocatalyst. Furthermore, photoluminescence (PL) spectra with terephthalic acid (TA) as a probe molecule were used to disclose the formation of $^{\bullet}OH$ on the surface of photocatalyst under visible-light irradiation. In a brief experimental procedure, photocatalyst (0.05 g) was dispersed in a 40 mL of the TA (5×10^{-4} mol L^{-1}) aqueous solution with NaOH (2×10^{-3} mol L^{-1}) at room temperature. The above suspension was subjected for the photocatalytic activity evaluation of the catalyst under visible-light irradiation and the PL intensity measured using a fluorescence spectrophotometer with excitation wavelength of 365 nm.

2.6 Electrochemical impedance spectroscopy (EIS)

EIS measurements were performed on an electrochemical workstation (ZAHNER IM6e Electrik, Germany) based on a conventional three-electrode system comprised of carbon paste as the working electrode, platinum wire as the counter electrode, and Ag/AgCl (3 N KCl) as the reference electrode. The EIS were performed in a 0.1 M Na_2SO_4 solution containing 5 mM $[Fe(CN)_6]^{3-}/[Fe(CN)_6]^{4-}$ with a frequency range from 0.01 Hz to 100 kHz at 0.24 V, and the amplitude of the applied sine wave potential in each case was 5 mV.

3. Results and discussion

3.1 Formation of N-doped ZnO/g-C_3N_4 hybrid core–shell nanoplates

The general pathway used to prepare N-doped ZnO/g-C_3N_4 hybrid core–shell structures is shown in Scheme 1. The formation sequences are as follows. Stage 1: N-doped ZnO nanoplates were prepared *via* a simple calcination method from zinc oxalate as a precursor and urea as a N source. However, the zinc oxalate precursor was prepared by a co-precipitation method using zinc acetate and ammonium oxalate as the starting materials. Stage 2: first, the exfoliated sheet structure of g-C_3N_4 prepared by direct heating of the melamine under N_2 atmosphere is dispersed in water solvent by sonicating at the ambient temperature for 1 h. Second, the N-doped ZnO nanoplates (stage 1) were introduced into the exfoliated g-C_3N_4 dispersion. As time progresses these exfoliated sheets spontaneously coat the N-doped ZnO nanoplates to minimize the surface energy by forming core–shell nanoplates after 48 h,

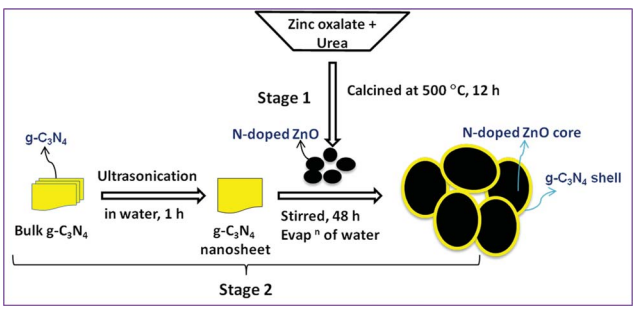

Scheme 1 Schematic illustration of the preparation of N-doped ZnO/g-C_3N_4 core–shell nanoplates.

resulting the formation of a heterojunction at the interface of g-C_3N_4 and N-doped ZnO.

3.2 Characterization

The content of g-C_3N_4 shell in the N-doped ZnO/g-C_3N_4 hybrid core–shell nanoplates was determined by thermogravimetric analysis (TG/DTA) as shown in Fig. S1.† The weight loss region can be seen in the N-doped ZnO/g-C_3N_4 hybrid core–shell sample. The decomposition of g-C_3N_4 starts at 550 °C and is completed at ~720 °C which can be attributed to the burning of g-C_3N_4.[34] Therefore, the g-C_3N_4 content in the hybrid core–shell nanoplates was easily determined from the corresponding weight loss. It is found 5.4 wt% and this amount is nearly consistent with the dosage of g-C_3N_4 in the hybrid sample.

The XRD pattern of ZnO, N-doped ZnO, g-C_3N_4 and N-doped ZnO/g-C_3N_4 samples were shown in Fig. 1. It can be seen from Fig. 1a that the diffraction pattern of N-doped ZnO was broader than that of pure ZnO. A significant diffraction peak broadening after N doping indicates a decreasing crystallinity due to incorporation of nitrogen into the ZnO. Moreover, the diffraction peak positions for N-doped ZnO are located at slightly higher angles than those for ZnO, suggesting an overall contraction of the lattice parameters as shown in Fig. 1b.[13] All the reflections in pure ZnO and N-doped ZnO can be readily indexed as the hexagonal Wurtize structure (JPCDS#36-1451). For graphitic carbon nitride (g-C_3N_4), a strong peak at $2\theta = 27.5°$ corresponding to the characteristic inter planar staking peak (002) of aromatic system is observed.[34] This characteristic peak was also presented in the N-doped ZnO/g-C_3N_4 core–shell nanostructure (see the inset of Fig. 1). It is also seen that the crystal phase of N-doped ZnO did not change after hybridization with g-C_3N_4 but the diffraction peak positions for N-doped ZnO/g-C_3N_4 are located at slightly lower angles than those for N-doped ZnO, suggesting a strong interaction between N-doped ZnO and g-C_3N_4. The intensity of the g-C_3N_4 peak in the composite increased with the content of loaded g-C_3N_4. Moreover, no other impurity phase was seen, indicating the N-doped ZnO/g-C_3N_4 is a two phase composite.

Fig. 2 shows the FTIR spectra of ZnO, N-doped ZnO, g-C_3N_4 and N-doped ZnO/g-C_3N_4 samples. The peaks in the region from 400 to 550 cm^{-1} of ZnO and N-doped ZnO is corresponding to Zn–O bending vibrations. In the FTIR spectrum of g-C_3N_4, the peaks at 1243 cm^{-1} and 1637 cm^{-1} were corresponding to the C–N and C=N stretching vibrations, respectively. The peak at 808 cm^{-1} was related to the s-triazine ring vibrations.[20] It can be seen clearly that the main characteristic peaks of g-C_3N_4 and N-doped ZnO presented in the N-doped ZnO/g-C_3N_4 hybrid core–shell nanoplates. It can also be seen that these main characteristic peaks of g-C_3N_4 shifted to a lower wave number in the hybrid core–shell nanoplates (Fig. 2b). The red shift in the bands, suggesting that the bond strengths of C–N and C=N were weakened *i.e.* the conjugated system of C_3N_4 was stretched and a more widely conjugated system containing C_3N_4 and ZnO appeared. The FTIR spectra show the presence of a C_3N_4 structure and it is an evidence of a covalent bond between C_3N_4 and ZnO.[35] This bond may be of significance to transfer carriers and promote a synergetic effect to enhance the photocatalytic activity.

The morphology and nanostructures of these samples were then investigated by FESEM and TEM. Fig. 3 shows typical SEM images of the prepared different samples. Fig. 3a shows the sheet structures of pure g-C_3N_4 after ultrasonic treatment. Fig. 3b shows the FESEM image of N-doped ZnO sample. It can be seen that the N-doped ZnO nanoplates have a relatively uniform diameter of about 50 nm. Fig. 3c and d show the low- and high-magnification FESEM images of the CNZON5 nanoplates, respectively. It can be seen that the CNZON5 nanoplates also have a relatively uniform diameter of about 55 nm. However, the FESEM images have not enough resolution for analysis of the core–shell structure. The amount of N in the N-doped ZnO nanoplates was also determined by elemental analysis (EDAX) as shown in Fig. S2† and 0.5 atomic weight percentage of N was found.

Fig. 4 shows the TEM images of the prepared different samples. Fig. 4b shows the TEM image of the g-C_3N_4 nanosheet with soft edges after exfoliating the bulk g-C_3N_4 (Fig. 4a). The SAED pattern of g-C_3N_4 nanosheet shows a full diffraction ring which can be indexed as the 002 reflection of g-C_3N_4, indicating that the material consists of extremely small crystallites which are randomly oriented (inset of Fig. 4b).[36] Fig. 4c shows the TEM image of N-doped ZnO nanoplates with average size of 50 nm. Fig. 5a and b show the TEM and HRTEM images of the CNZON5 core–shell nanoplates. The thickness of the g-C_3N_4 layer coated

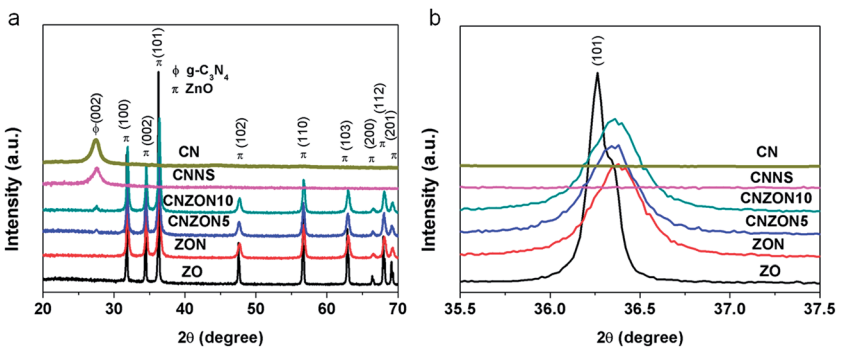

Fig. 1 XRD patterns of the prepared g-C_3N_4, ZnO, N-doped ZnO and N-doped ZnO/g-C_3N_4 photocatalysts (a) and the Bragg angle shift of 101 peak (b).

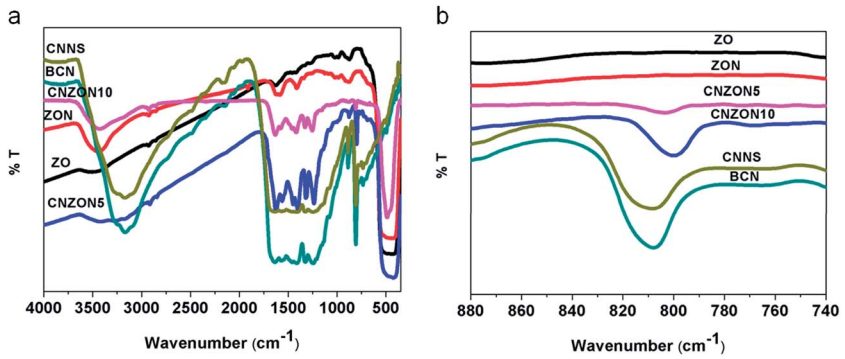

Fig. 2 FTIR spectra of the prepared g-C_3N_4, ZnO, N-doped ZnO and N-doped ZnO/g-C_3N_4 photocatalysts (a) and the peak shift in N-doped ZnO after hybridisation with g-C_3N_4 (b).

on the N-doped ZnO is about 3 nm for CNZON5. It can be also seen from Fig. 5b, the lattice structure of N-doped ZnO possess high order. The outer layer of the as-prepared N-doped ZnO/g-C_3N_4 sample was distinctly different from the N-doped ZnO core. The measured interplanar spacing of the core is 0.24 nm which corresponds to the ZnO (101) plane and the measured interplanar spacing of the shell is 0.32 nm (inset of Fig. 5b) which corresponds to the g-C_3N_4 (002) plane. Fig. 5c shows the core–shell morphology of CNZON10, which is prepared with 10 wt% of g-C_3N_4 to N-doped ZnO. As can be seen from Fig. 5d, for CNZON10, the g-C_3N_4 shell is thicker, ~6 nm. Therefore, it is observed that the thickness of the g-C_3N_4 shells increases with increasing the wt% of g-C_3N_4 to N-doped ZnO.

X-ray photoelectron spectroscopy (XPS) measurements were carried out to know the chemical states of C, N, Zn, and O species in the as-prepared samples. Fig. S3† shows the survey scan XPS spectra of N-doped ZnO sample, which indicates the presence of Zn, O, and N in the N-doped ZnO. High resolution spectra of Zn2p, O1s, and N1s are shown in Fig. 6a–c. As shown in Fig. 6a, the binding energy values of Zn $2p_{3/2}$ and Zn $2p_{5/2}$ are

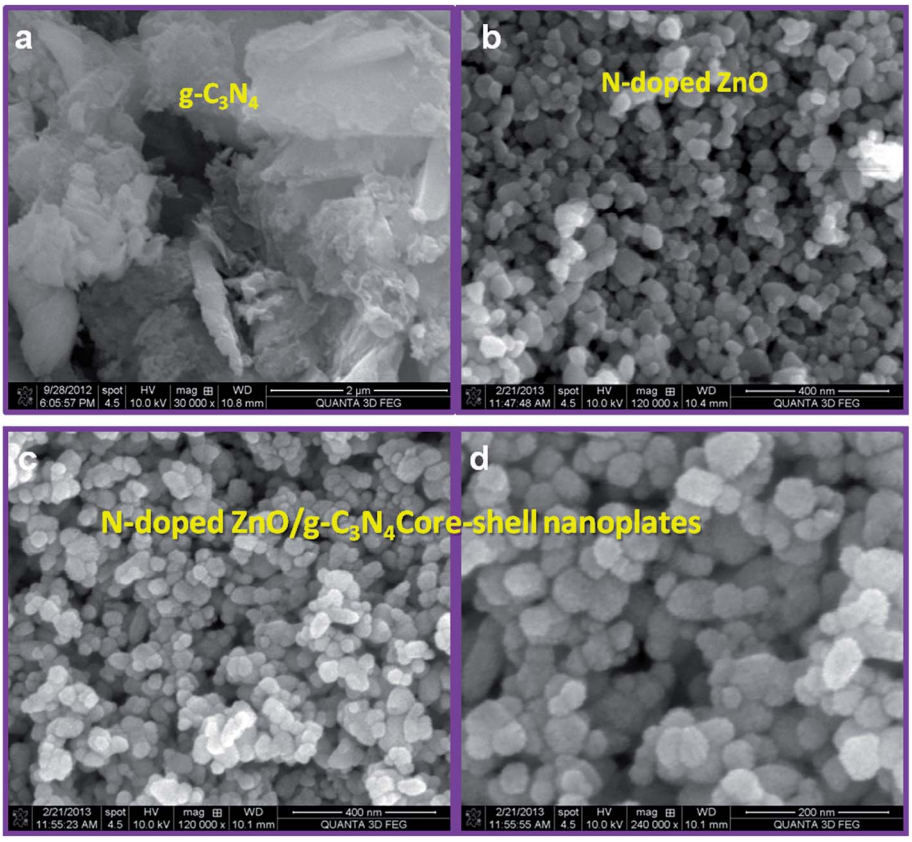

Fig. 3 FESEM images of the prepared g-C_3N_4, N-doped ZnO and N-doped ZnO/g-C_3N_4 photocatalysts: (a) bulk g-C_3N_4, (b) N-doped ZnO, (c) CNZON5 and (d) CNZON5 (magnified).

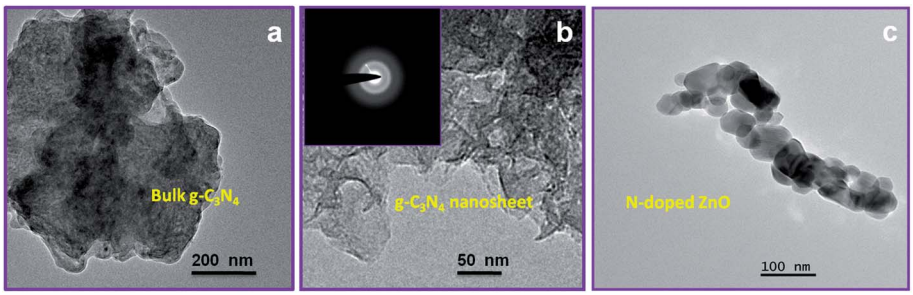

Fig. 4 TEM images of the prepared photocatalysts: (a) bulk g-C_3N_4, (b) g-C_3N_4 nanosheet (inset figure shows the SAED pattern of g-C_3N_4 nanosheet), (c) N-doped ZnO.

observed at 1021.96 eV and 1045.01 eV, respectively, suggesting the typical binding energies of Zn^{2+}.[14,20] The O1s peak at 530.31 eV is mainly assigned to the oxygen atoms coordinated with Zn atoms (Fig. 6b). The other O1s peak at 531.70 eV is associated with the presence of an OH group or a water molecule on the surface of N-doped ZnO/g-C_3N_4 core–shell composite.[14] In the N1s spectrum (Fig. 6c), the N1s peak at a binding energy of 398.3 eV can be assigned to nitrogen (Zn–N).[13,14] Therefore, N is successfully doped at the O sites of ZnO.

Fig. S4† shows the survey scan XPS spectra of the N-doped ZnO/g-C_3N_4 (5.4%) composite samples. The results indicate the presence of Zn, O, C, and N in the N-doped ZnO/g-C_3N_4 (5.4%) core–shell composite. High resolution spectra of Zn2p, O1s, C1s, and N1s are shown in Fig. 7a–d. However, the binding energy values of Zn $2p_{3/2}$ and Zn $2p_{5/2}$ in the N-doped ZnO/g-C_3N_4 (5.4%) composite are observed at 1021.78 eV and 1044.81 eV, which are slightly lower than those for pure N-doped ZnO (Fig. 7a). The binding energy values of O1s in the N-doped ZnO/g-C_3N_4 (5.4%) composite are observed at 530.11 eV and 531.40 eV that are also slightly lower than those for pure N-doped ZnO (Fig. 7b). Such a shift may be attributed to the interaction between N-doped ZnO and g-C_3N_4. Fig. 7c shows the carbon (1s) spectrum, which can be fitted into 2 peaks at 284.3, and 285.8 eV. The C1s peak at 285.4 eV is assigned to a C–N–C coordination. The other C1s peak at 284.6 eV is attributed to the adventitious carbon on the surface of N-doped ZnO/g-C_3N_4 composite photocatalyst.[37] N1s spectrum (Fig. 7d) can also be fitted into three peaks. The main N1s peak at a binding energy

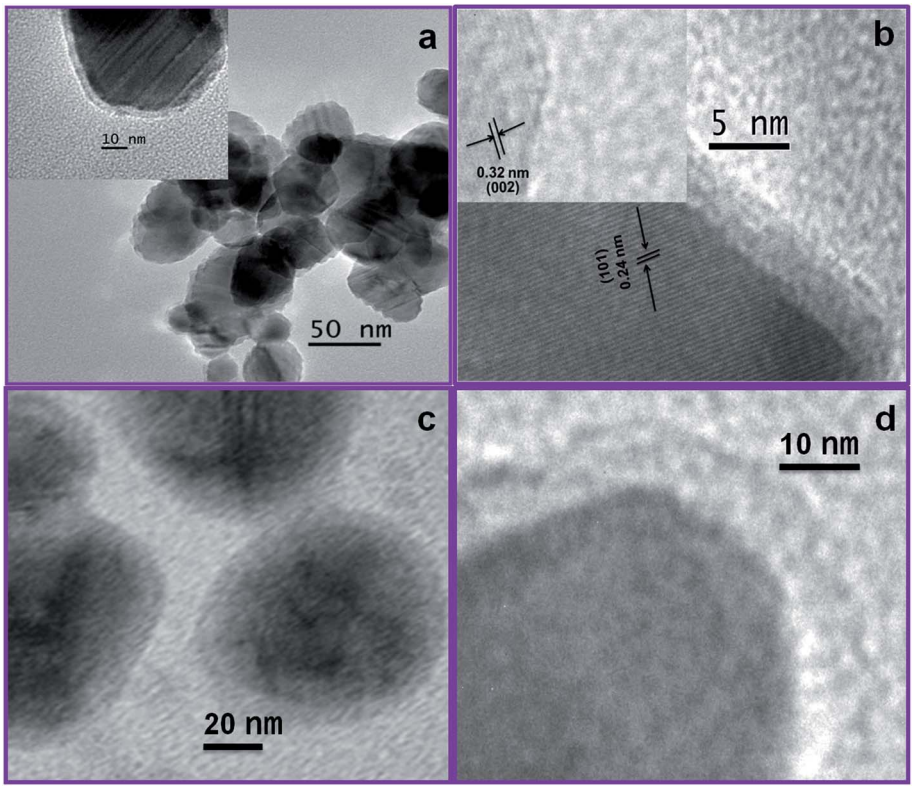

Fig. 5 TEM and HRTEM images of the prepared N-doped ZnO/g-C_3N_4 core–shell photocatalysts: (a) TEM image of CNZON5, (b) HRTEM image of CNZON5, (c) TEM image of CNZON10 and (d) HRTEM image of CNZON10.

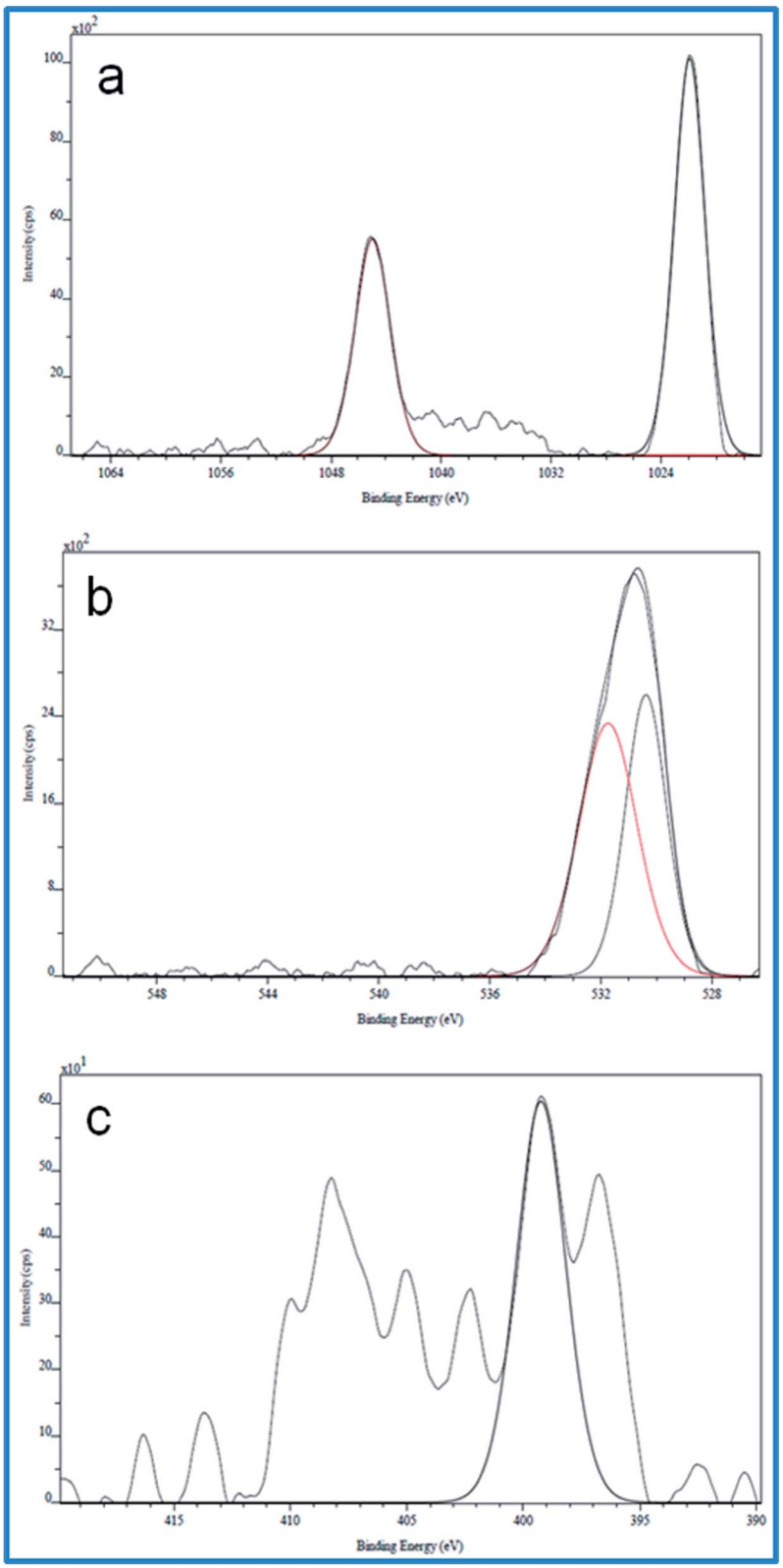

Fig. 6 XPS spectra of N-doped ZnO: (a) Zn 2p, (b) O1s, (c) N1s.

of 398.7 eV can be assigned to sp^2-hybridized nitrogen (Zn–N) and (C═N–C).[14,37] The other peaks at 400.8 eV are attributed to quaternary nitrogen.[37] Therefore, with the combination of the XRD, SEM-EDS, TEM and XPS investigation, the results confirmed that there were both N-doped ZnO and g-C_3N_4 species in the heterojunction structure.

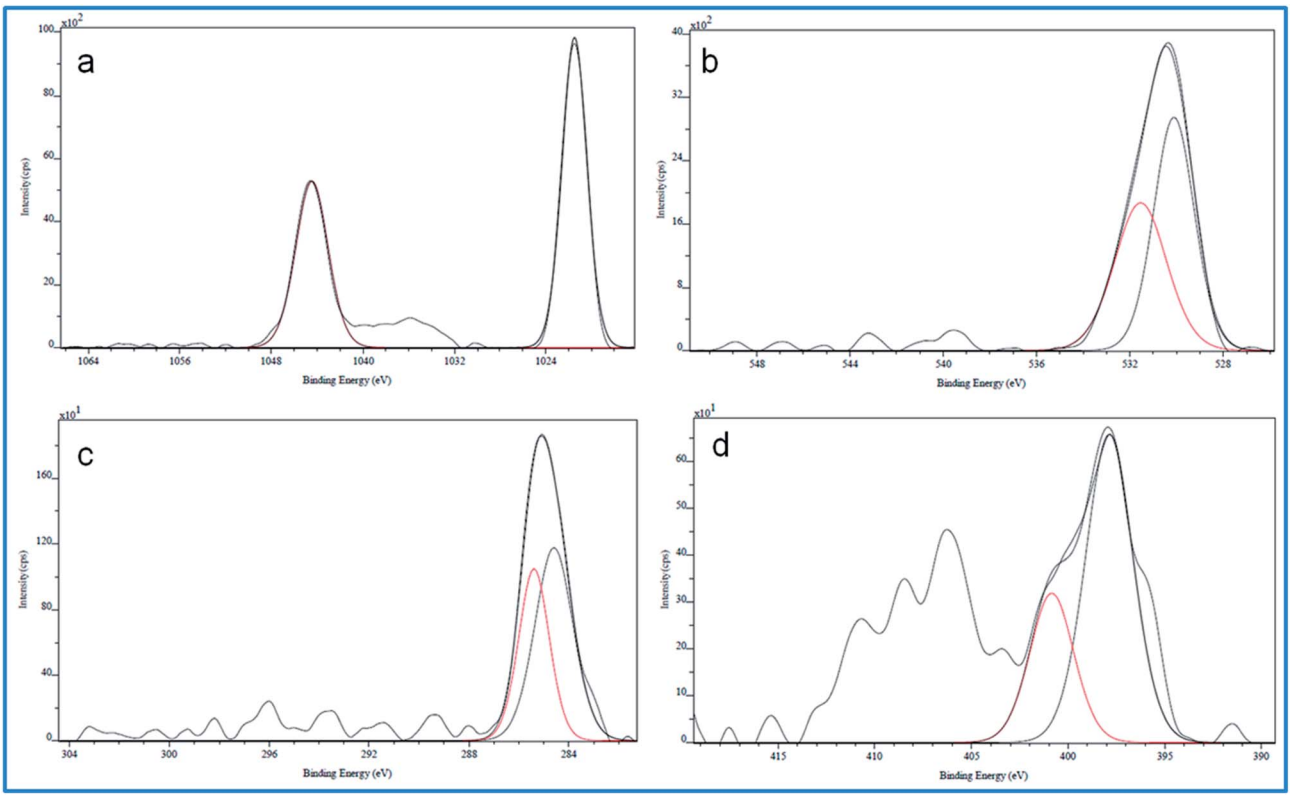

Fig. 7 XPS spectra of N-doped ZnO/g-C_3N_4: (a) Zn 2p, (b) O1s, (c) C1s (d) N1s.

The UV-Vis DRS spectra of the prepared different samples are shown in Fig. 8. As expected, a sharp fundamental absorption cut off edge at 385 nm for ZnO appeared, corresponding to a band gap of 3.25 eV, whereas g-C_3N_4 nanosheet has an absorption cut off edge at 454 nm, corresponding to a band gap of 2.73 eV showing a red shift from its bulk counterpart (2.69 eV). As shown in Fig. 8, after nitrogen doping, the band gap of ZnO is reduced from 3.25 to 3.14 eV and the contribution of nitrogen to the top of the valence band (VB) of ZnO can play an important role *i.e.* driving the absorption of N-doped ZnO to the visible region. Further N-doped ZnO/g-C_3N_4 (3.06 eV for CNZON5 and 2.99 eV for CNZON10) shows the broader absorption edge and extends to the visible region as compared to that of N-doped ZnO due to the presence of g-C_3N_4 on the N-doped ZnO surface. It is notable that compared with N-doped ZnO surface, the absorption edge of N-doped ZnO/g-C_3N_4 experiences a red-shift of about 10–20 nm. However, these band gap energies estimated by using Kubelka–Munk function as shown in Fig. S5.†[38] The valence band edge potential and the conduction band edge potential of a semiconductor material can be determined by using the following equation:[39]

$$E_{VB} = X - E_e + 0.5E_g \quad (1)$$

$$E_{CB} = E_{VB} - E_g \quad (2)$$

where E_{VB} is the valence band edge potential, X is the absolute electronegativity of the semiconductor, which is determined as the geometric mean of the electronegativity of the constituent atoms, E_e is the energy of free electrons on the hydrogen scale (~4.5 eV) and E_g is the band gap energy of the semiconductor. The E_{CB} of N-doped ZnO and g-C_3N_4 are calculated and found to be −0.17 eV and −1.22 eV, respectively. The E_{VB} of N-doped ZnO and g-C_3N_4 are estimated to be 2.97 and 1.51 eV, respectively.

The specific surface area of N-doped ZnO and N-doped ZnO/g-C_3N_4 samples were investigated by nitrogen adsorption–desorption analysis, as shown in Fig. 9. The specific surface area of N-doped ZnO/g-C_3N_4 core–shell nanoplates is 45.17 $m^2\ g^{-1}$ which is much higher than that of N-doped ZnO nanoplates

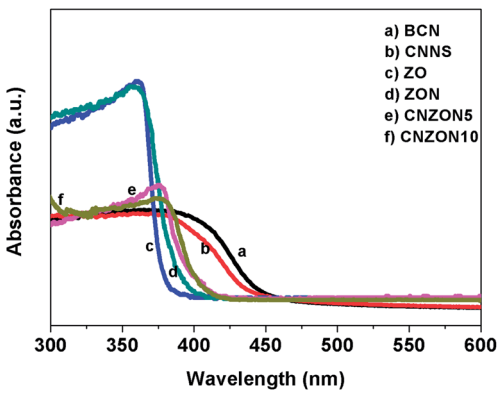

Fig. 8 UV-Vis DRS spectra of the prepared g-C_3N_4, ZnO, N-doped ZnO and N-doped ZnO/g-C_3N_4 photocatalysts.

(23.45 $m^2 g^{-1}$), and g-C_3N_4 (8 $m^2 g^{-1}$). Relatively, a large specific surface area of N-doped ZnO is useful for the better adsorption and also provides a higher number of reactive sites for photocatalytic process, thereby it has a significant contribution to the enhancement of the photocatalytic efficiency.

3.3 Photocatalytic performance

The photocatalytic activity of the prepared samples was evaluated *via* photodegradation of RhB under visible-light irradiation, as shown in Fig. 10. As can be seen from Fig. 10, the N-doped ZnO/g-C_3N_4 hybrid core–shell photocatalysts exhibited significantly higher photocatalytic activity for the photodegradation of RhB than that of pure g-C_3N_4 and N-doped ZnO. However, the simple photolysis of RhB was also examined for comparison under the same experimental conditions in the absence of catalyst and it was observed that the efficiency was negligible which indicates that RhB is stable under visible-light irradiation. The adsorption ability of the ZON and CNZON5 photocatalysts was also investigated in the dark condition for 30 min duration. The adsorption ability of CNZON5 photocatalyst was significantly higher than that of pure ZON photocatalyst, indicating the adsorption of RhB in the composite system is not simple physical adsorption but it is also contributed from π–π stacking between RhB and g-C_3N_4 which is similar to the conjugation between aromatic molecules and graphene.[40] The results show that both light and catalyst are necessary for the effective photodegradation of RhB. The experimental data were fitted in the pseudo first-order kinetic equation $\ln(C/C_0) = -kt$ (Fig. 10b). The apparent rate constant of RhB photodegradation is about 0.0679 min^{-1} for CNZON5 and 0.0441 min^{-1} for CNZON10 core–shell nanoplates. The optimum photocatalytic activity of CNZON5 is more than 10 times higher than that of ZON (0.0065 min^{-1}) and almost 5 times higher than that of g-C_3N_4 nanosheets (0.0140 min^{-1}). Moreover, the rate of CNZON5 core–shell nanoplates is forty times higher than that of pure ZnO (0.0014 min^{-1}) and 6 times higher than that of bulk g-C_3N_4 under visible-light irradiation. The results imply that ZnO/g-C_3N_4 hybrid core–shell is a much better photocatalyst than that of pure ZnO or g-C_3N_4. The enhanced photocatalytic activity may be due to a significant synergistic effect at the interface of the g-C_3N_4 and N-doped ZnO.

3.4 EIS

In addition, EIS measurement was carried out to investigate the charge transfer resistance and the separation efficiency of the photoinduced charge carrier in the core–shell photocatalyst. As can be seen from Fig. 11, the diameter of the Nyquist semicircle for the core–shell photocatalyst is smaller than that of g-C_3N_4 and N-doped ZnO which indicates that the core–shell photocatalyst has a lower resistance than that of g-C_3N_4 and N-doped ZnO. This result demonstrates that the interface of the N-doped ZnO/g-C_3N_4 can enhance the separation and transfer efficiency of photoinduced electron–hole pairs[40] which is favourable condition for improving the photocatalytic activity.

3.5 Proposed photocatalytic mechanism

3.5.1 Role of reactive species. In general, many reactive species including h^+, $^{\bullet}OH$ and $O_2^{\bullet-}$ are expected to be involved in the photocatalytic reaction. The effects of some scavengers and N_2 purging on the photodegradation of RhB were examined in an attempt to propose the possible photocatalytic reaction mechanism. The tertiary butyl alcohol (*t*BuOH), N_2 purging and ammonium oxalate (AO) were used as $^{\bullet}OH$, $O_2^{\bullet-}$ and h^+ scavengers, respectively.[33,41] As shown in Fig. 12a, the photocatalytic activity of the hybrid core–shell nanoplates was greatly suppressed by the addition of *t*BuOH as $^{\bullet}OH$ scavenger, indicating that $^{\bullet}OH$ is the main active species in the photocatalytic reaction. A significant decrease in the photocatalytic activity was also observed by the addition of AO as h^+ scavenger and N_2 purging as $O_2^{\bullet-}$ scavenger, respectively. It is suggested that $O_2^{\bullet-}$ and h^+ play an almost equally important role in the photocatalytic reaction. In summary, the main reactive species involved in the photocatalytic degradation of RhB over the core–shell photocatalyst are $^{\bullet}OH$, $O_2^{\bullet-}$ and h^+. Moreover, the formation of $^{\bullet}OH$ during the photocatalytic reaction under visible-light irradiation was confirmed by the photoluminescence spectra with terephthalic acid (TA) as a probe molecule as shown in Fig. 12b. The details of the experimental procedures have been reported in some earlier reports.[42,43] The results show that an obvious photoluminescence signal at about 425 nm of 2-hydroxy terephthalic acid is observed. The peak intensity of the photocatalyst increases with the increase in the irradiation time, suggesting that a high formation rate of $^{\bullet}OH$

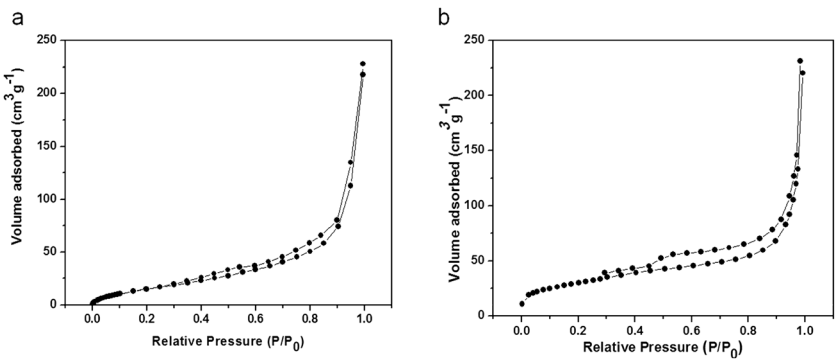

Fig. 9 Nitrogen adsorption–desorption isotherm, and specific surface area of the prepared (a) N-doped ZnO and (b) CNZON5 photocatalysts.

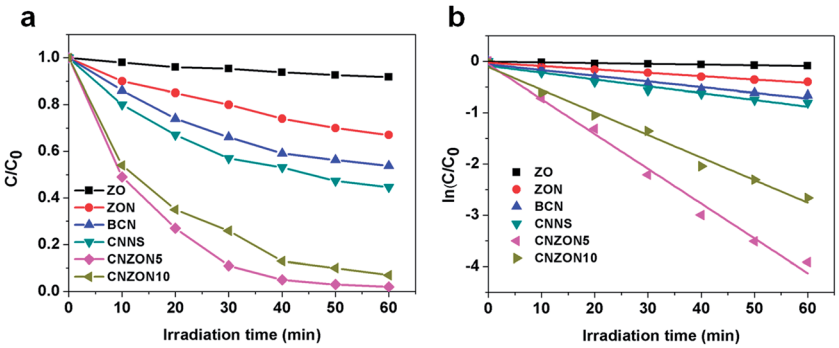

Fig. 10 (a) Photocatalytic activity for the degradation of RhB solution by using pure ZnO, N-doped ZnO, g-C_3N_4 and N-doped ZnO/g-C_3N_4 photocatalyst under visible-light irradiation; (b) The ln(C/C_0) *vs.* time curves.

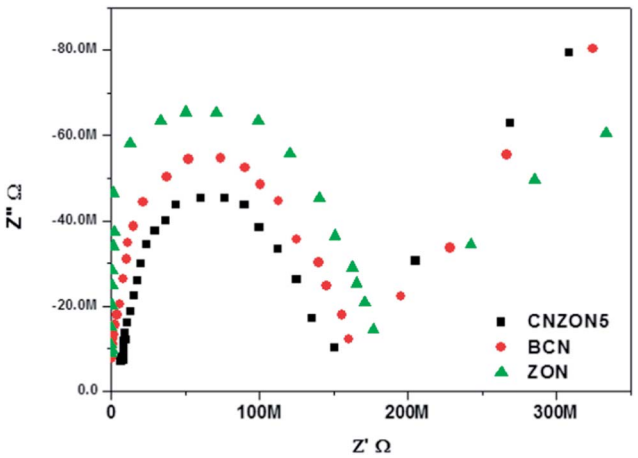

Fig. 11 EIS profile of N-doped ZnO, g-C_3N_4 and N-doped ZnO/g-C_3N_4 photocatalyst.

on the surface of the photocatalyst and results in higher photocatalytic activity. It is also in good agreement with the results of *t*BuOH quenching.

3.5.2 Proposed mechanism. On the basis of above results, a possible photocatalytic mechanism for the photodegradation of RhB over N-doped ZnO/g-C_3N_4 core–shell photocatalyst is proposed. The most common separation process of photoinduced electron–hole pairs for a great number of composite photocatalysts is shown in Fig. 13a. If the photoinduced electron–hole pair separation in the N-doped ZnO/g-C_3N_4 photocatalyst is as according to Fig. 13a, the photoinduced electrons in the CB of g-C_3N_4 can migrate to the CB of N-doped ZnO, and the photoinduced holes in the VB of N-doped ZnO can migrate to the VB of g-C_3N_4. Unfortunately, these accumulated electrons in the conduction band of N-doped ZnO cannot produce $O_2^{\bullet-}$ from dissolved O_2 by photoreduction process, because the conduction edge potential of N-doped ZnO (−0.2 eV *vs.* NHE) is more positive than the standard redox potential $E^0_{(O_2/O_2^{\bullet-})}$ (−0.3 eV *vs.* NHE). Meanwhile, the photoinduced holes of g-C_3N_4 also cannot oxidize the adsorbed H_2O molecules to $^{\bullet}OH$ because the valance edge potential of g-C_3N_4 (+1.3 eV *vs.* NHE) is more negative than the standard redox potential $E^0_{(^{\bullet}OH/H_2O)}$ (+2.8 eV *vs.* NHE), suggesting that the charge carrier transfer in accordance with the most common model (Fig. 13a) is not favorable for the generation of the main reactive species $O_2^{\bullet-}$ and $^{\bullet}OH$, resulting in a lower photocatalytic activity for the N-doped ZnO/g-C_3N_4 photocatalyst. However, under the experimental conditions, the results show the presence of $O_2^{\bullet-}$ and $^{\bullet}OH$, the strong oxidizability of h^+ and the high photocatalytic activity. So the photoinduced electron–hole separation process is proposed *via* Z-scheme mechanism, as shown in Fig. 13b. Namely, the photoexcited electrons in the CB of N-doped ZnO

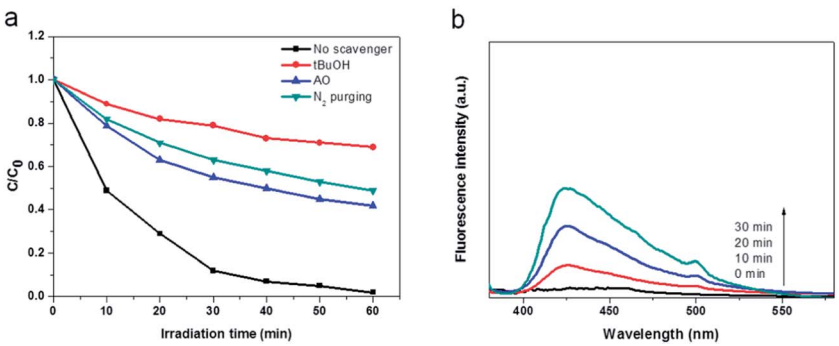

Fig. 12 (a) Effects of different scavengers on the degradation of RhB in the presence of N-doped ZnO/g-C_3N_4 core–shell photocatalyst under visible-light irradiation. (b) $^{\bullet}OH$ trapping PL spectra of ZnO/g-C_3N_4 core–shell photocatalyst with TA solution under visible-light irradiation.

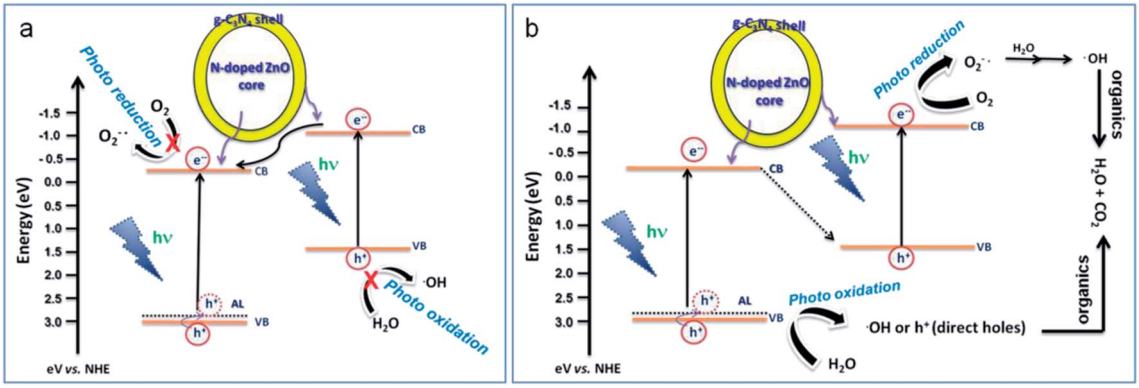

Fig. 13 Schematic diagram illustrating the mechanism for photoinduced charge carrier transfer in most common composites (not Z-scheme photocatalysts) (a) and N-doped ZnO/g-C_3N_4 core–shell (Z-scheme photocatalysts) (a) under visible-light irradiation.

transfer to the VB of g-C_3N_4 quickly, resulting in the combination of the electrons in the CB of N-doped ZnO and photoexcited holes in the VB of g-C_3N_4, and accumulated rich electrons in the CB of g-C_3N_4 and holes in the VB of N-doped ZnO participate in the reduction and oxidation reactions, respectively. As a result, the electrons in the CB of g-C_3N_4 have more negative potential to reduce the molecular oxygen to yield $O_2^{\bullet-}$, which then induces the degradation of RhB.[3] The holes in the valance band of N-doped ZnO have more positive potential to generate abundant active $^{\bullet}OH$ with powerful oxidization capability. Therefore, the photocatalytic activity is significantly promoted, and RhB is degraded through the $O_2^{\bullet-}$ and $^{\bullet}OH$ or direct h^+ oxidation pathway. According to the results, it is proposed Z-scheme mechanism that shows the real separation process of photoinduced electron–hole pairs. Therefore, the N-doped ZnO/g-C_3N_4 system is a type of Z-scheme photocatalyst under our experimental conditions.

3.5.3 ESR measurements. ESR measurements were carried out to confirm the generation of $O_2^{\bullet-}$ to prove the rationality of the proposed photocatalytic reaction mechanism. DMPO in methanol was used for the detection of $O_2^{\bullet-}$.[44,45] No obvious peaks of $O_2^{\bullet-}$ are observed in the ESR pattern for pure N-doped ZnO as shown in Fig. 14a. However, the strong characteristic peaks of $O_2^{\bullet-}$ are observed for the N-doped ZnO/g-C_3N_4 core–shell sample and the weaker peaks of $O_2^{\bullet-}$ are also observed for pure N-doped ZnO. It is clear that $O_2^{\bullet-}$ is produced in the process of photocatalytic reaction over N-doped ZnO/g-C_3N_4 core–shell photocatalyst under visible light irradiation. These ESR results clearly suggested that the N-doped ZnO/g-C_3N_4 core–shell sample is more favourable for the formation of $O_2^{\bullet-}$ than that of pure N-doped ZnO and g-C_3N_4 samples. Based on the ESR results, it can be concluded that the transfer of the photoinduced charge carriers is according to Fig. 13b in the N-doped ZnO/g-C_3N_4 system.

3.5.4 Photoluminescence. It is well known that the photoluminescence emission spectra results from the recombination of free carriers.[46,47] In order to determine the role of photoinduced electron–hole pairs in the as-prepared core–shell sample and understand the proposed mechanism, photoluminescence studies were carried out. Fig. 14b shows the PL spectra of ZnO, N-doped ZnO, g-C_3N_4 and N-doped ZnO/g-C_3N_4 photocatalyst with an excitation wavelength of 365 nm at room temperature. It can be seen that the pure g-C_3N_4 and ZnO have a strong emission peak around 460 nm and 510 nm, respectively. However, after N incorporation into the ZnO crystal structure, the photoluminescence intensity was greatly suppressed, suggesting that the recombination rate of the photoinduced electron–hole in N-doped ZnO is lower than that of pure ZnO. The result means that lower photoluminescence intensity indicates a higher photocatalytic activity under the experimental conditions. It is notable that the change in intensity agrees well with that of the photocatalytic activity of the N-doped ZnO as shown in Fig. 10. Furthermore, after hybridization of N-doped ZnO with g-C_3N_4 (N-doped ZnO/g-C_3N_4 core–shell), the photoluminescence intensity has slightly increased and is higher than that of pure N-doped ZnO. This is opposite to that of general photoluminescence experiments. The reason may be that, as it is well known, the photoluminescence peak intensities are strongly dependent on the recombination of photoinduced electron–hole pairs. In theory, if the photoexcited electrons and holes are transferred as shown in Fig. 13a, the photoluminescence intensity of the N-doped ZnO/g-C_3N_4 core–shell nanoplates must be lower than that of pure N-doped ZnO because the photoinduced electrons and holes of g-C_3N_4 and N-doped ZnO are separated effectively. However, the results show that the photoexcited electrons and holes are not transferred as shown in Fig. 13a. In contrast, as shown in Fig. 13b, the higher photoluminescence intensities of the samples are attributed to the higher recombination rate between photoexcited electrons in the CB of N-doped ZnO and photoexcited holes in the VB of g-C_3N_4, suggesting that the rich electrons in the CB of g-C_3N_4 with more negative potential and holes in the VB of N-doped ZnO with more positive potential undergo reduction and oxidation reactions to produce $O_2^{\bullet-}$ and $^{\bullet}OH$, respectively, so the photocatalytic activity of N-doped ZnO/g-C_3N_4 core–shell nanoplates is significantly improved. Based on the analysis, it is clear that the recombination and transfer of photoinduced electrons and holes for the core–shell photocatalyst are indeed as shown in Fig. 13b *i.e.* N-doped ZnO/g-C_3N_4

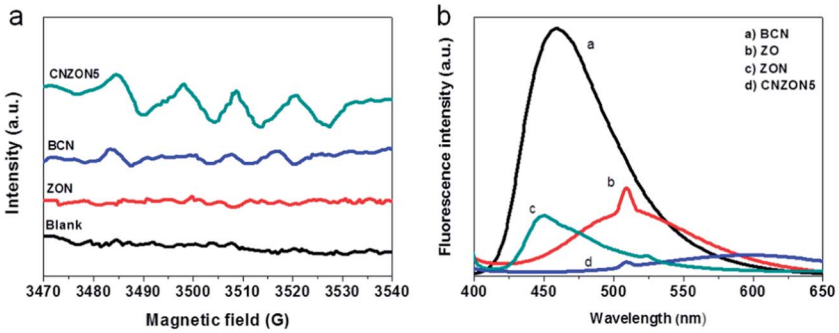

Fig. 14 (a) ESR signals of DMPO–$O_2^{\bullet-}$ with irradiation for 20 s in methanol dispersion. (b) Room temperature photoluminescence spectra (excited at 365 nm) of pure ZnO, N-doped ZnO, g-C_3N_4 and N-doped ZnO/g-C_3N_4 photocatalyst under visible-light irradiation.

core–shell photocatalyst is a typical Z-scheme photocatalyst with high photocatalytic oxidation and reduction performance.

3.6 Reusability

For the practical applications, it is necessary to investigate the long-term stability of a photocatalyst during photocatalytic reaction. To study the reusability of the N-doped ZnO/g-C_3N_4 hybrid core–shell photocatalyst, six successive photocatalytic experiments were carried out by adding used CNZON5 photocatalyst to fresh RhB solutions under visible-light irradiation. However, the concentration of catalyst and RhB in the solution remained constant for each cycle. The photocatalytic activity of CNZON5 is retaining over 90% of its original activity value after six successive experimental runs under the same experimental conditions as shown in Fig. 15. The XRD and FTIR spectra were recorded for the reused hybrid core–shell photocatalyst and no change was observed in the resulting spectra which indicates the high structural stability of N-doped ZnO/g-C_3N_4 (ESI, Fig. S6†). The N-doped ZnO/g-C_3N_4 hybrid nanocomposite photocatalysts can be easily reused by a simple filtration or by low-speed centrifugation and thus avoiding the second pollution. Therefore, g-C_3N_4/N-doped ZnO composites can be used as high-performance visible-light photocatalysts and for potential applications in environmental protection.

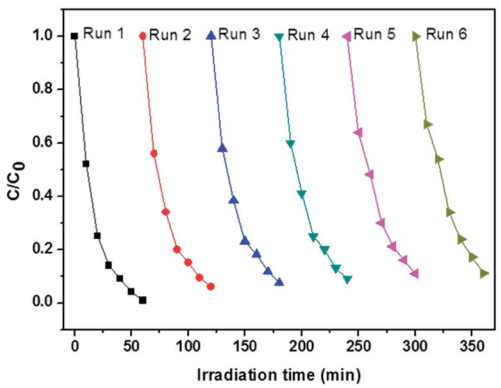

Fig. 15 Recyclability of the CNZON5 photocatalyst for the degradation of RhB under visible-light irradiation (six successive experimental runs).

4. Conclusion

In summary, we have successfully prepared N-doped ZnO/g-C_3N_4 hybrid core–shell nanoplates *via* a facile ultrasonic dispersion method. Significantly, the enhanced visible-light photocatalysis is achieved due to the prolonged life time of charge carrier transfer at the interface of N-doped ZnO/g-C_3N_4. Direct Z-scheme mechanism is proposed for the prolonged life time of charge carrier transfer at the interface of N-doped ZnO/g-C_3N_4 by trapping experiments of photoinduced electrons and holes under visible-light irradiation. More importantly, the as-prepared N-doped ZnO/g-C_3N_4 hybrid core–shell nanostructure possesses high photostability. This ideally versatile hybrid core–shell nanostructure prepared from a cost-effective and environmentally friendly process would be useful for various applications, including catalysis, drug delivery system, sensors, photonics and energy storage and conversion.

Acknowledgements

The corresponding author thanks the Department of Science and Technology, Government of India for financial support (SR/FT/CS-096/2009). Santosh Kumar thanks the Ministry of Human Resource Development, Government of India for providing fellowship. Authors also thank Prof. A. K. Ganguli, Indian Institute of Technology Delhi, for carrying out part of this work in his lab.

References

1 M. R. Hoffmann, S. T. Martin, C. Wonyong and D. W. Bahnemannt, *Chem. Rev.*, 1995, **95**, 69.
2 V. K. Prashant, *J. Phys. Chem. C*, 2007, **111**, 2834.
3 K. Rajeshwara, M. E. Osugi, W. Chanmanee, C. R. Chenthamarakshan, M. V. B. Zanoni, P. Kajitvichyanukul and R. Krishnan-Ayer, *J. Photochem. Photobiol., C*, 2008, **9**, 171.
4 R. M. Mohamed, D. L. McKinney and W. M. Sigmund, *Mater. Sci. Eng., R*, 2012, **73**, 1.
5 C. Xiaobo, S. Shaohua, G. Liejin and S. M. Samuel, *Chem. Rev.*, 2010, **110**, 6503.

6 S. Li, F. Zheng, S. Cai, W. Liang and Y. Li, *Sens. Actuators, B*, 2013, **188**, 280.
7 C. Janáky, K. Rajeshwar, N. R. de Tacconi, W. Chanmanee and M. N. Huda, *Catal. Today*, 2013, **199**, 53.
8 S. Rehman, R. Ullah, A. M. Butt and N. D. Gohar, *J. Hazard. Mater.*, 2009, **170**, 560.
9 T. Chungui, Z. Qi, W. Aiping, J. Meijia, L. Zhenglan, J. Baojiang and F. Honggang, *Chem. Commun.*, 2012, **48**, 2858.
10 K. Maeda, T. Takata, M. Hara, N. Saito, Y. Inoue, H. Kobayashi and K. Domen, *J. Am. Chem. Soc.*, 2005, **127**, 8286.
11 L. Zhaoyang, B. Hongwei, X. Shiping and D. S. Darren, *Int. J. Hydrogen Energy*, 2011, **36**, 13473.
12 P. Yin, Q. Shuchun, W. Wan-Sheng and X. An-Wu, *CrystEngComm*, 2013, **15**, 6518.
13 Z. Xu, S. Chenghua, Y. Hua, G. C. Zhi, X. Zheng, Y. Delai, Q. L. Gao, L. Xinyong and W. Lianzhou, *J. Phys. Chem. C*, 2013, **117**, 4937.
14 S. Chen, W. Zhao, S. Zhang and W. Liu, *Chem. Eng. J.*, 2009, **148**, 263.
15 Q. Hongchun, L. Weiying, X. Yujing and H. Tao, *ACS Appl. Mater. Interfaces*, 2011, **3**, 3152.
16 H. Fu, T. Xu, S. Zhu and Y. Zhu, *Environ. Sci. Technol.*, 2008, **42**, 8064.
17 Y. Guidong, J. Zheng, S. Huahong, X. Tiancun and Y. Zifeng, *J. Mater. Chem.*, 2010, **20**, 5301.
18 X. Fang, Y. Yafei, H. Huijuan, W. Dapeng, G. Zhiyong and J. Kai, *CrystEngComm*, 2012, **14**, 3615.
19 W. Jinfeng, T. Takuya, T. Bin, H. Xueliang, S. Lu and W. Xungai, *ACS Appl. Mater. Interfaces*, 2012, **4**, 3084.
20 W. Yajun, S. Rui, L. Jie and Z. Yongfa, *Energy Environ. Sci.*, 2011, **4**, 2922.
21 Z. Liwu, C. Hanyun, Z. Ruilong and Z. Yongfa, *J. Phys. Chem. C*, 2009, **113**, 2368.
22 Z. Hao, Z. Ruilong and Z. Yongfa, *J. Phys. Chem. C*, 2009, **113**, 4605.
23 W. Xinchen, K. Maeda, A. Thomas, K. Takanabe, X. Gang, J. M. Carlsson, K. Domenm and M. Antonietti, *Nat. Mater.*, 2008, **8**, 76.
24 S. Kumar, T. Surendar, B. Kumar, A. Baruah and V. Shanker, *J. Phys. Chem. C*, 2013, **117**(49), 26135.
25 G. C. Rajib and P. Santanu, *Chem. Rev.*, 2012, **112**, 2373.
26 P. Chengsi, X. Jing, W. Yajun, L. Di and Z. Yongfa, *Adv. Funct. Mater.*, 2012, **22**, 1518.
27 K. Sunita, K. Simanta, P. Amitava and A. K. Ganguli, *J. Phys. Chem. C*, 2012, **116**, 23653.
28 W. Xuewen, L. Gang, Q. L. Gao and C. Hui-Ming, *Int. J. Hydrogen Energy*, 2010, **35**, 8199.
29 K. Maeda, L. Daling and K. Domen, *ACS Catal.*, 2013, **3**, 1026.
30 X. Lin, M. P. S. Ellen and E. S. Sara, *J. Phys. Chem. C*, 2012, **116**, 871.
31 F. Ning, J. Zhiliang, W. Yuqi, L. Gongxuan and L. Dongyang, *J. Phys. Chem. C*, 2011, **115**, 8586.
32 J. Y. Hyeong, L. Hyunjoo, D. K. Nam, M. L. David, Y. Sungju and Y. Jongheop, *ACS Nano*, 2011, **5**, 4084.
33 S. Kumar, T. Surendar, A. Baruah and V. Shanker, *J. Mater. Chem. A*, 2013, **1**, 5333.
34 S. Kumar, B. Kumar, T. Surendar and V. Shanker, *Mater. Res. Bull.*, 2014, **49**, 310.
35 L. Wei, W. Mingliang, X. Chunxiang and C. Shifu, *Chem. Eng. J.*, 2012, **209**, 386.
36 Y. Zhang, Q. Pan, G. Chai, M. Liang, G. Dong, Q. Zhang and J. Qiu, *Sci. Rep.*, 2013, **3**, 1943.
37 N. Xiao, D. Lau, W. Shi, J. Zhu, X. Dong, H. H. Hng and Q. Yan, *Carbon*, 2013, **57**, 184.
38 A. Srinivasan, O. Naoki and M. Masahiro, *Appl. Catal., B*, 2010, **100**, 502.
39 L. Yongyu, W. Jianshe, Y. Hongchang, D. Liyun and L. Zhongjun, *J. Mol. Catal. A: Chem.*, 2011, **334**, 116.
40 H. Zhang, L. Xiaojun, L. Yueming, Y. Wang and L. Jinghong, *ACS Nano*, 2010, **4**, 380.
41 X. Tongguang, Z. Liwu, C. Hanyunm and Z. Yongfa, *Appl. Catal., B*, 2011, **101**, 382.
42 B. Cheng, L. Yao and Y. Jiaguo, *J. Hazard. Mater.*, 2010, **177**, 971.
43 I. Ken-ichi, A. Fujishima, T. Watanabe and K. Hashimoto, *Electrochem. Commun.*, 2000, **2**, 207.
44 H. Ji, F. Chang, X. Hu, W. Qin and J. Shen, *Chem. Eng. J.*, 2013, **218**, 183.
45 C. Shifu, J. Lei, T. Wenming and F. Xianliang, *Dalton Trans.*, 2013, **42**, 10759.
46 J. Liqiang, Q. Yichun, B. Wang, L. Shudan, J. Baojiang, L. Yang, F. Wei, F. Honggang and S. Jiazhong, *Sol. Energy Mater. Sol. Cells*, 2006, **90**, 1773.
47 F. Xianliang, T. Wenming, J. Lei and C. Shifu, *Chem. Eng. J.*, 2012, **180**, 170.

